

Adaptive imaging system using image quality metric based on statistical analysis of speckle fields

Dai Hyun Kim^a, Kirill Kolesnikov^a, Andrew Kostrzewski^a, Gajendra Savant^a, Anatoly A. Vasiliev^b, and Mikhail A. Vorontsov^c

^aPhysical Optics Corporation, 20600 Gramercy Place, Bldg. 100, Torrance, CA 90501

^bOptiMight Communications, Inc, Mountain View, CA 94043

^cArmy Research Laboratory, Adelphi, MD 20783

ABSTRACT

This paper describes an Opto-Silicon Adaptive Imaging (OSAI) system capable of operating at low light intensities with high resolution, high accuracy, wide dynamic range, and high speed. The system consists of three major subsystems: (a) an adaptive imaging system in which a liquid crystal wavefront corrector measures image quality based on statistical analysis of a speckle field; (b) an image quality analyzer (IQA); (c) an opto-silicon multi-chip module (MCM) combining a high-resolution ferroelectric liquid crystal (FLC) SLM, CCD photodetector array, field-programmable gate array (FPGA), and digital signal processor (DSP). The OSAI wavefront control applies adaptive optoelectronic feedback for iterative wavefront restoration and distortion compensation, using an image quality metric based on statistical properties of the speckle field produced by moving a diffuser in the Fourier transform plane of an IQA optical system. A prototype IQA system was designed, manufactured, and tested using an input liquid crystal SLM, a Fourier lens, a light-shaping diffuser, and an output photodiode.

Keywords: Adaptive optics, Wavefront control

1. INTRODUCTION

Adaptive optic systems are commonly used to compensate for atmospheric turbulence-induced wavefront distortions in astronomical and ground-to-ground imaging systems.¹⁻⁵ Even more significant phase distortion can affect long-path interferometers and remote-sensing laser systems operating in a phase-distorting medium, but adaptive optics are rarely used in these systems because of their cost and complexity. In a typical high-resolution adaptive optical system, the number of wavefront control channels $N=10^5$ is restricted either by the number of photons available in astronomy or by the resolution and dynamic range of wavefront sensors and phase correctors. Another limiting factor is the size mismatch between the wavefront sensor and the corrector, since the additional imaging system introduces additional aberrations. Finally, most adaptive optics algorithms and systems are designed to correct distorted point light sources in astronomic applications rather than compensating for distortions of extended sources. For all these reasons, *it would be impossible to increase the resolution of adaptive optical systems by a factor of 400 or more without rethinking the adaptive system architecture and the associated control algorithms.*

In a typical adaptive-optic wavefront control system, a phase corrector -- an active mirror or spatial light modulator (SLM) -- corrects the aberrations of wavefronts distorted by the atmosphere or an optical system.¹⁻⁵ The measure of image quality at a 2-D wavefront sensor using a photodetector array is fed back to adjust the phase modulation function of the SLM. With the recent appearance of inexpensive, high-resolution wavefront correctors such as liquid crystal (LC) multi-element phase modulators,⁶ LC television (LCTV) panels,⁷⁻⁹ and micro-electromechanical systems (MEMS) mirrors,^{10,11} adaptive wavefront control and interferometry have become promising and cost-effective adaptive optics technologies. Traditional adaptive optics systems directly measure the distorted wavefront, continuously correcting any mismatch between the measured wavefront and a known reference wavefront;^{4,5} they thus require *a priori* knowledge of or direct access to the reference source. State-of-the-art high-resolution adaptive optical systems apply optimization algorithms based on image quality criteria;¹⁻³ they do not require a reference object, and are therefore preferable for ground-to-ground and air-to-ground imaging of arbitrary extended objects. These systems, however, lack advanced optoelectronic VLSI technology to interface a high-resolution phase corrector and an optically and electronically matched photodetector array to the control computer.

Such a technology will significantly improve the computational capabilities of adaptive optical systems, combining the massive parallelism of optical processing with the programmability and complex functionality of VLSI electronics.

This paper describes an Opto-Silicon Adaptive Imaging (OSAI) integrated adaptive optical system capable of operating at low light intensities with high resolution, high accuracy, wide dynamic range, and high speed. The wavefront control includes an adaptive imaging system based on a statistical analysis of the speckle field implemented using opto-silicon multi-chip module (MCM) technology combining a high-resolution ferroelectric liquid crystal (FLC) SLM, CCD photodetector array, field-programmable gate array (FPGA), and digital signal processing (DSP).

2. OPTO-SILICON ADAPTIVE IMAGING WAVEFRONT CONTROL

The OSAI wavefront control system architecture is illustrated in Figure 1. The system consists of two major subsystems: (a) an adaptive imaging system in which a liquid crystal wavefront corrector measures image quality based on statistical analysis of a speckle field;¹⁻³ (b) an opto-silicon multi-chip module (MCM) combining a high-resolution ferroelectric liquid crystal SLM, CCD photodetector array, field-programmable gate array, and digital signal processor. The OSAI wavefront control applies adaptive optoelectronic feedback for iterative wavefront restoration and distortion compensation, using an image quality metric and parallel perturbation algorithm. The system illustrated in Figure 1 implements stochastic parallel gradient descent optimization, which is the best for high-resolution adaptive optics.^{12,13} In effect, this algorithm performs gradient descent with a maximum attainable average convergence speed, a factor of $N^{1/2}$ faster than for conventional gradient descent based on sequential perturbations.¹⁴⁻¹⁶ The greatest benefit for adaptive optics applications may come from the fact that the parallel perturbation technique is well suited to analog VLSI implementation.¹⁷

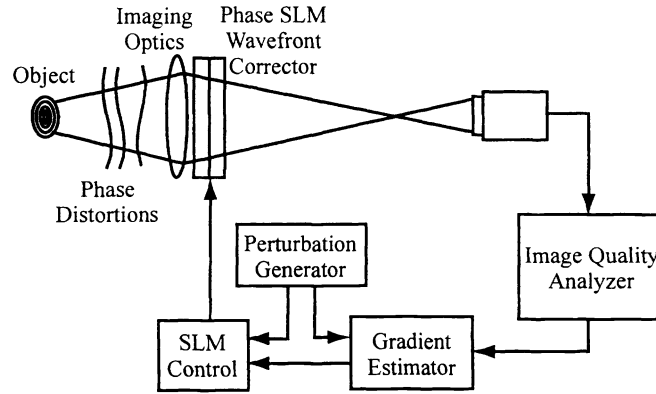


Figure 1. OSAI wavefront control system architecture.

The OSAI wavefront control consists of an incoherent adaptive imaging system with a random aberration $\phi(r)$ located in the exit pupil, an image quality analyzer, a high-resolution wavefront corrector, and a digital processing module. A fast video camera at the imaging system output captures a distorted image $I(r)$ (where $r = \{x, y\}$ is the coordinate vector) that enters the image quality analyzer (IQA). The IQA can either measure or calculate an image quality metric $j = j(u_1, \dots, u_j, \dots, u_N)$, where u_j , $j = 1, \dots, N$, are wavefront control parameters.

In the image quality analyzer of Figure 2, the distorted image $I(r)$ from the CCD in Figure 1 is fed to a phase SLM in the back focal plane of a Fourier transform lens with focal length F_l and illuminated with a plane wave A_0 . This produces a phase-modulated wave with complex amplitude $f_{ph}(r) = A_0 \exp[i\alpha l(r)]$, where α is the slope of the SLM phase modulation curve. We denote $F_{ph}(k)$ the Fourier transform $F\{f_{ph}(r)\}$ of the phase-modulated input $F_{ph}(r)$; then the intensity in the back focal plane is given by

$$I_{ph}(r_F) \propto |F(r_F)|^2, \quad (1)$$

where $k = \{k_\lambda, k_y\} = k r_F / F_l$, $k = 2\pi/\lambda$, λ is the wavelength, and r_F is a coordinate vector in the back focal plane (Fourier plane).¹⁸ The effective width b_{ph} of the intensity distribution (1) represents an image quality criterion^{1,2} given by

$$b_{ph} = \iint \sqrt{(k_x^2 + k_y^2) I_{ph}(k)} d^2k / \iint I_{ph}(k) d^2k . \quad (2)$$

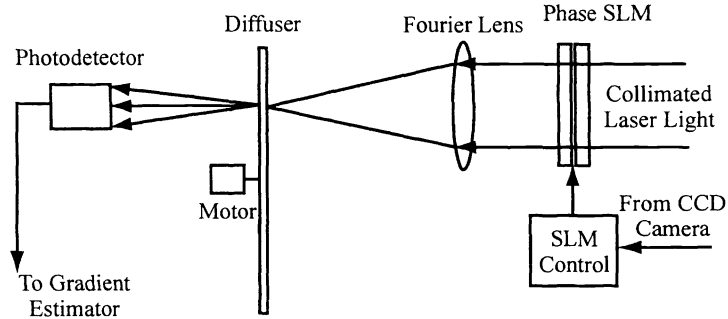


Figure 2. Optoelectronics for image quality analyzer.

In general, a good-quality image preserves fine details and has a relatively wide spatial spectrum compared to a distorted image, though there are exceptions to this rule, especially among images with periodic structure such as texture images.

To measure the image quality according to criterion (2), we estimate the characteristic size r_s of a speckle pattern generated by a rotating diffuser in the Fourier plane of the IQA optical system. The characteristic speckle size at a distance z from the diffuser is given by¹⁹

$$r_s \sim z\lambda/b_{ph} . \quad (3)$$

Hence, the wider the image spatial spectrum the smaller the speckle size in the photodetector plane of the IQA system illustrated in Figure 2. Therefore, the statistical properties of the speckle field yield an accurate and useful estimate of the image quality. Specifically, we use the variance of the photodetector output produced by rotating a diffuser in the Fourier plane of the IQA optical system as the image quality criterion:¹

$$J_{ph} = \sigma^2 = \iint I_{ph}^2(r_F) d^2r_F . \quad (4)$$

A single photodiode interfaced to the gradient estimator is the output device. With a CCD camera in the IQA output plane, we can also measure speckle size by calculating the auto-correlation functions of the intensity distribution in the speckle pattern.¹⁹ Figure 3 identifies the electronic hardware for image quality measurement and parallel gradient descent optimization.

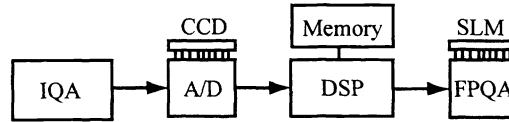


Figure 3. OSAI digital processing components.

3. IMAGE QUALITY ANALYSER

We used the phase SLM from an Epson Crystal Image video projector as the input device for the experimental IQA system diagrammed in Figure 2. The pixel count of an Epson liquid crystal SLM is 320×240 , with a 1.25-inch diagonal clear aperture. Each pixel measures $55 \mu\text{m} \times 60 \mu\text{m}$, with a center-to-center spacing of $80 \mu\text{m} \times 90 \mu\text{m}$. The pixel pitch of the Epson SLM corresponds to a 46% active area. The total transmission efficiency of the device is about 43% at $\lambda = 0.6328 \mu\text{m}$.

3.1. Test and Evaluation of Phase SLM

The optical test setup for measuring the Epson SLM phase modulation is shown schematically in Figure 4. The test optical system includes an Ealing LDL175 diode laser (633 nm wavelength, 0.9 mW power), a Newport three-axis spatial filter, a PAC088 Newport precision optimized achromatic doublet ($D = 50.8 \text{ mm}$, $F = 250 \text{ mm}$) collimating lens, and a CoHU 1100 CCD camera. The Fourier lens is a 01LAO288 Melles Griot precision optimized achromatic doublet ($D = 63.0 \text{ mm}$,

$F = 400$ mm), and the microscope objective is a Newport M-20X objective lens. The polarizers included with the projector were replaced with high-quality Melles Griot polarizers when used in the optical systems discussed here. The polarizers were aligned along the long molecular axes of the LC at the LCD substrates, resulting in pure phase modulation of the transmitted light with particular settings of the SLM controls.

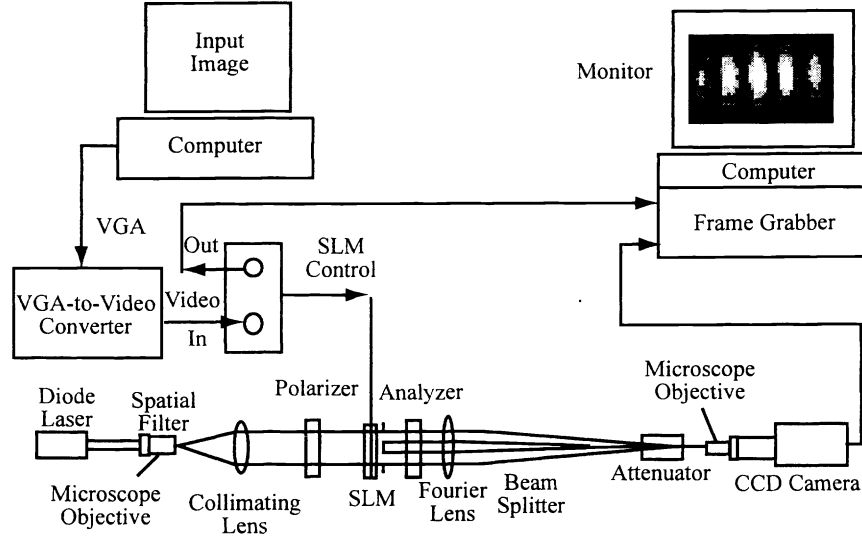


Figure 4. Test setup for measuring phase modulation of Epson SLMs.

Light from the laser diode was expanded by the Newport M-60X objective lens and filtered through a $5\text{-}\mu\text{m}$ pinhole diaphragm. The collimated light beam illuminated an SLM set between a pair of polarizers in front of the Fourier transform lens. A mask with two identical rectangular windows was placed behind the SLM. Computer-generated 640×480 test images were fed to the SLM VGA output of a computer. They were gray-scale intensity distributions with uniform zero level in the right half and 0 to 256 (0,15,31,...,255) uniform gray scale levels in the left half of the image. The mask separates the two regions of the SLM area, generating interference fringes in the Fourier transform plane given by¹⁸

$$\left| F(k_x, k_y) \right|^2 = \frac{(ab)^2 \sin(ak_x/2) \sin(ak_x/2)}{k_x k_y} \left[(\delta A)^2 + 4(A^2 + A\delta A) \cos^2(k_x \Delta X / 2 + \phi / 2) \right], \quad (5)$$

where a and b are the window width and height, ϕ is the phase modulation, A is the SLM transmittance for those pixels where modulation is zero, and δA is the transmittance change due to the residual amplitude modulation. The fringes move as the phase modulation varies. The modulation depth of the fringe pattern can be derived from Eq. (6), yielding visibility

$$v = \frac{I_1}{I_0} = \frac{2A(A + \delta A)}{(\delta A)^2 + 2A(A + \delta A)} = \frac{2m}{1 + m^2}, \quad (6)$$

where I_0 and I_1 are the zero-order (dc) and first-order Fourier components of the interference pattern, and $m = 1 + \delta A / A$ is the amplitude modulation. Hence, the visibility varies if amplitude modulation of the transmitted light occurs. The Newport M-20X objective lens magnifies the interference pattern. The Fourier transform intensity is registered using the CCD camera in the Fourier transform plane. Digital post-processing of the interference pattern calculates the phase and amplitude modulation of the SLM.

We measured the phase modulation and visibility of four Epson SLM devices for various input signal levels and brightness settings. The tint and color controls were always set at 50% of maximum. We used MATLAB to calculate the phase and amplitude modulation vs. gray scale level, using interference measurements. The results for the best SLM are shown in Figure 5.

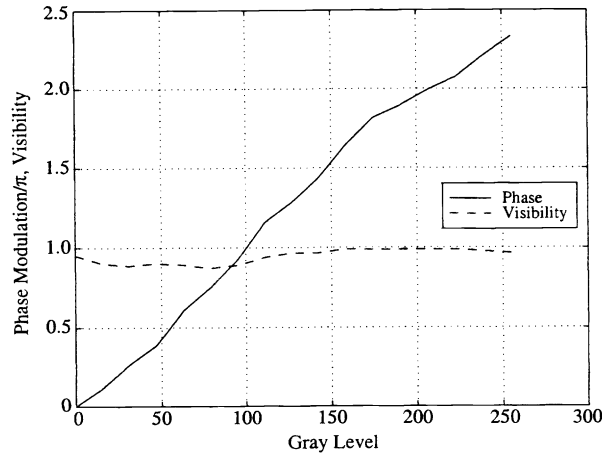


Figure 5. Phase modulation and visibility vs. gray level for the maximum input signal 0.46 V peak-to-peak (gray level 255) and LCD brightness 0.29 max.

The curves in Figure 5 show linear phase modulation $> 2\pi$ (linearity 80% rms) and visibility > 0.8 with the chosen control settings.

3.2. Image Quality Criterion Measurement

Figure 6 diagrams the Phase I image quality measurement system based on the Epson SLM whose modulation curves are shown in Figure 5. CCD camera 1 looks at the input image 0.8 m away. A 5 mm extension ring was used with a camera lens that has a 32 mm focal length and an aperture set at 5.6. We varied the focus distance of the camera lens from 0.25 m to infinity to control the input image quality, as shown in Table 1. Figure 7 shows input images and output speckle patterns for two focusing distances.

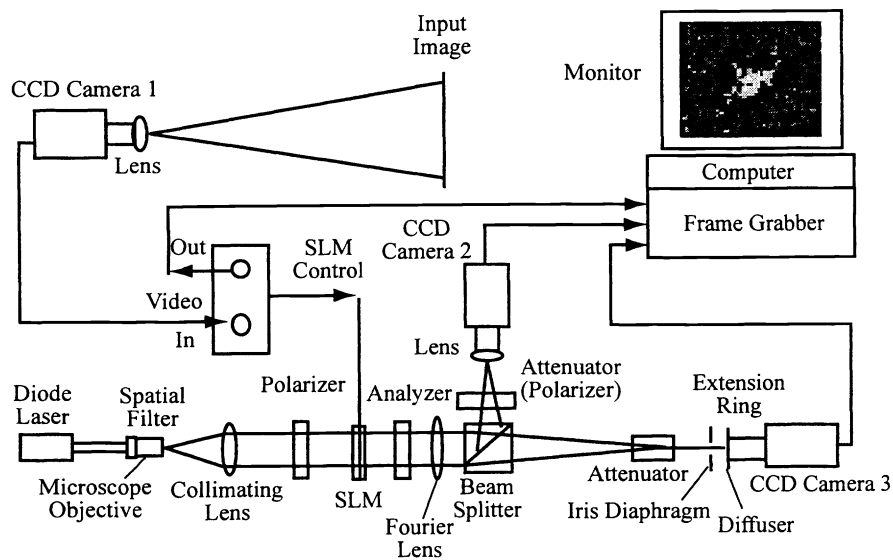


Figure 6. Image quality measurement test setup.

Table 1. Focus Distance of the Camera Lens and Corresponding Defocusing Parameter

Focus distance	∞	2 m	1 m	0.5 m	0.3 m	0.25 m
Defocusing	-1	0	1	2	3	4

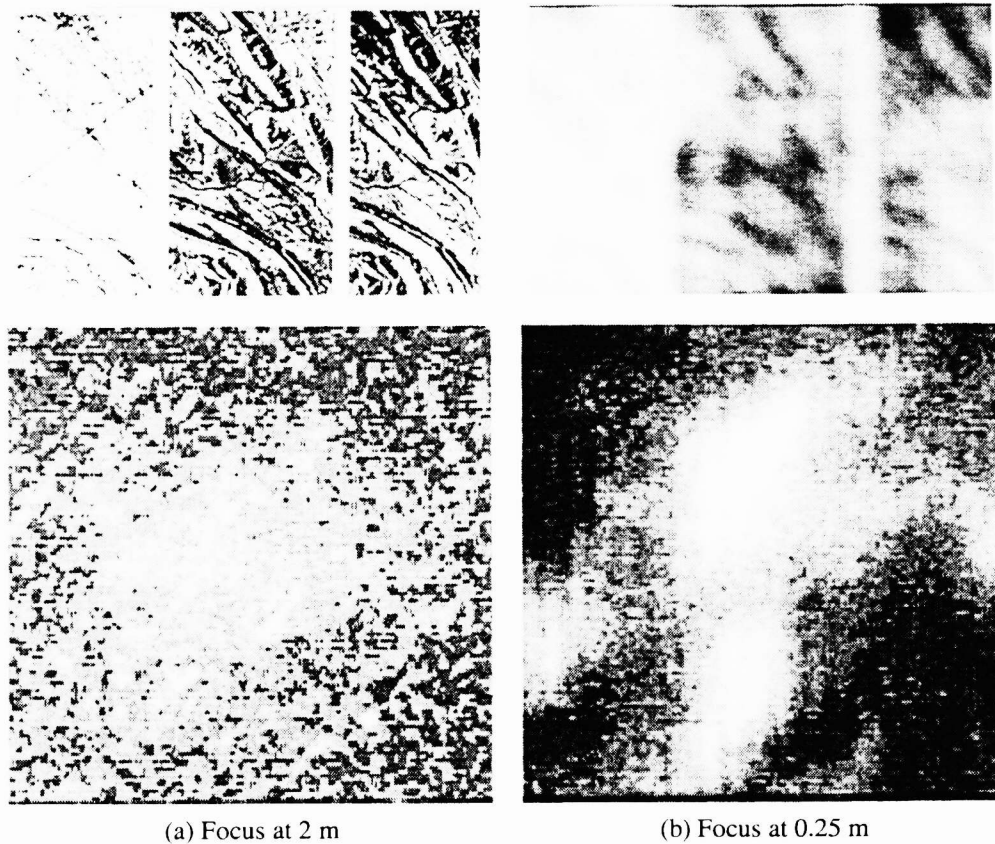


Figure 7. Input images and corresponding speckle patterns for two focusing settings of the input camera.

A POC Light Shaping Diffuser²⁰ was used to shape the speckle pattern, whose average size varies with the input image quality. The system includes an Ealing LDL175 diode laser (633 nm wavelength, 0.9 mW power), a Newport three-axis spatial filter, and a PAC088 Newport precision optimized achromatic doublet ($D = 50.8$ mm, $F = 250$ mm) collimating lens to form a collimated beam illuminating the SLM between crossed polarizers. The polarizers were aligned along the long molecular axes of the LC at the LCD substrates, producing pure phase modulation of the transmitted light with particular settings of the LCD controls. The Fourier lens is a 01LAO288 Melles Griot precision optimized achromatic doublet ($D = 63.0$ mm, $F = 400$ mm). A Cohu 1100 CCD camera is used to capture the output speckle patterns. The second CCD camera looks at the Fourier transform plane through a non-polarizing beam splitter.

The speckle patterns in Figure 7 shows average speckle size increasing with defocusing. To calculate the average speckle size, we used MATLAB FFT routines to compute the auto-correlation¹⁸ of the speckle patterns, and measured the correlation peak width at level 0.5 using the `contour` function in MATLAB, as shown in Figure 8. Figure 9 shows the average speckle size vs. defocusing.

The speckle size measurements yield an auto-correlation peak width-based image quality metric, which is robust and less sensitive to the photodetector noise and variations of the input illumination. Unfortunately, the correlation measurements require substantial computation, which can significantly slow the image quality metric computation.

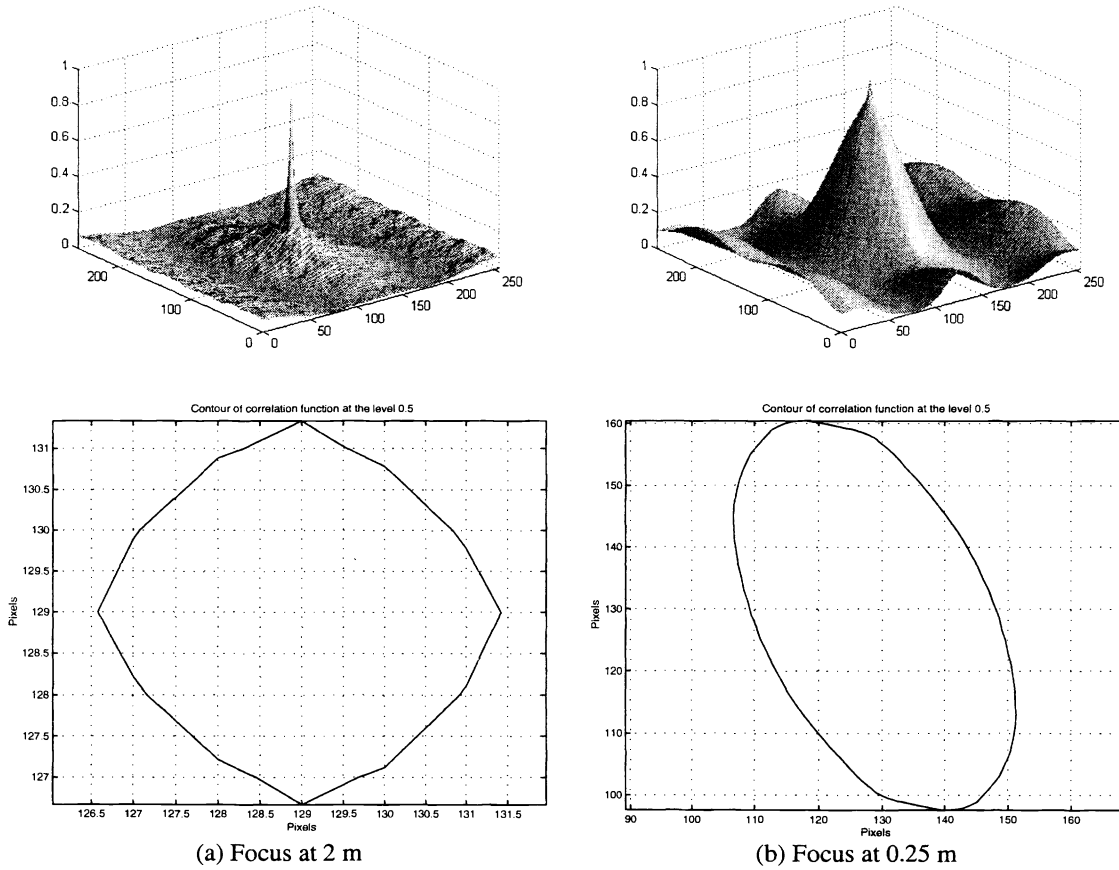


Figure 8. 3-D plots of auto-correlation functions in Figure 7 and the contours of the auto-correlation peaks at level 0.5.

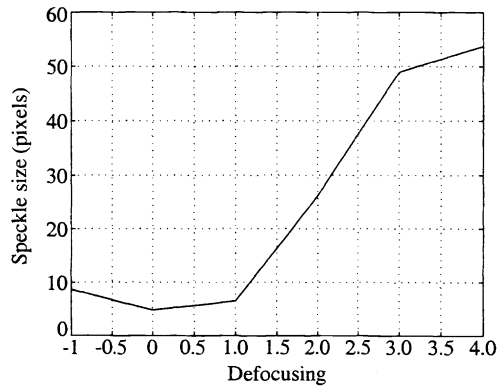


Figure 9. Average speckle size vs. defocusing.

3.3. Experimental Image Quality Analyzer System

An optical system for generating image-quality-dependent wavefront perturbations is shown in Figure 10. A coherent wave with complex amplitude $A(\mathbf{r})I_0^{1/2}(\mathbf{r})\exp[i\psi(\mathbf{r})]$ is focused on a rough surface (the light shaping diffuser in Figure 10), creating a speckle field $I_p(\mathbf{r})$ at the observation plane $z = L$ (photodiode). The power spectrum $G(\mathbf{p})$ for the speckle field intensity fluctuation is given by^{1,21}: $G(\mathbf{p}) = \iint I_s(\mathbf{r}_p)I_s(\mathbf{r}_F - L\mathbf{p}/k)d^2\mathbf{r}_F$, where $k = 2\pi/\lambda$ and $I_s(\mathbf{r})$ is the intensity distribution on

the rough surface. A beam splitter directs a portion of the modulated light to a lens that forms either the Fourier transform of the SLM plane or its image on a CCD camera.

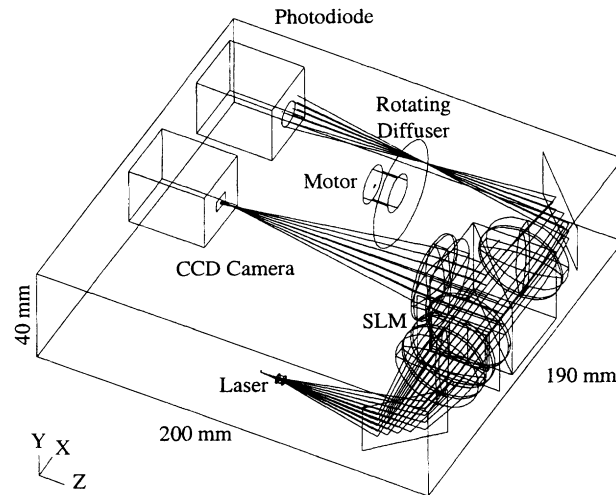


Figure 10. IQA optical system design and ray-trace.

Thus, to create a speckle field $I_p(r)$ with the intensity fluctuation power spectrum $G(p)$, we project the corresponding intensity distribution $I_s(r_F)$ onto the rough surface from an SLM in the back focal plane of the lens as shown in Figure 10. The SLM forms the input phase distributions $\Psi(r)$ to create the required intensity distribution $I_s(r_F)$ in the lens focal plane.

The speckle field is varied by moving the rough surface perpendicular to the direction of light propagation, i.e., by rotating the LSD in the focal plane. As shown in Figure 10, the wavefront is perturbed by transforming the speckle field intensity pattern into its corresponding phase modulation by means of a high-resolution phase modulator (wavefront corrector) connected with a camera. The great advantage of speckle-based perturbation is that perturbation statistics are easily controlled by changing the intensity distribution $I_s(r_F)$ during the adaptation process.

A single photodiode interfaced to the photo-current statistics estimator is used as the output device in this case. With a CCD camera in the IQA output plane, we can also measure speckle size by calculating the autocorrelation functions of the intensity distribution in the speckle pattern,^{18,19} A POC Light Shaping Diffuser is used to generate speckle patterns; the system otherwise consists of standard off-the-shelf optical components: a diode-laser light source, and a fast photodetector at the output. The output CCD camera can capture processed images or spatial power spectra.

In the experimental IQA setup (see Figure 11), coherent light from a Blue Sky Research PS020-00 CircuLaser™ diode laser is expanded by a Melles Griot 01LLD003 symmetric-concave precision grade lens (aperture $D = 6$ mm, focal length $F = -8$ mm), collimated by a Melles Griot 01LAL017 precision achromatic doublet lens ($D = 40$ mm, $F = 100$ mm), and illuminates the phase SLM. The SLM is placed between two crossed polarizers (Edmund Scientific F52557 mounted polarizing filters) to perform phase modulation as described in Section 3.1. Therefore, in passing through the liquid crystal layer the input wave acquires an additional phase modulation that is dependent on the intensity distribution in the distorted input image. Thus, the SLM converts the intensity distribution $I_s(r_F)$ corresponding to the distorted image into a phase distribution whose complex amplitude in the focal plane of the Fourier lens is proportional to the spatial spectrum of the field. The Fourier lens is a Melles Griot 01LAL017 precision achromatic doublet lens ($D = 40$ mm, $F = 100$ mm). The fluctuation of the output speckle field is measured with a photodiode receiver at a distance Z from the LSD to measure the image quality metric.¹⁻³ We used a New Focus 2031 silicon photodetector with 8 mm aperture, adjustable in three steps of conversion gain (1.2×10^3 V/W, 0.6×10^5 V/W, or 1.2×10^6 V/W) in the visible (400-1070 nm) wavelength range, and with cutoff frequencies of 1 MHz (low gain), 150 kHz (medium gain), or 90 kHz (high gain).

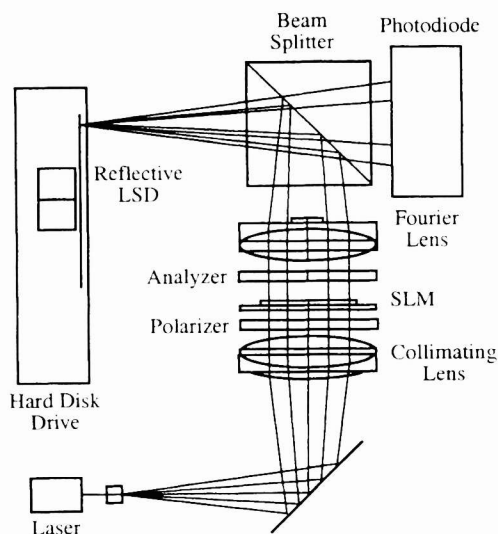


Figure 11. IQA optical system using reflective rotating LSD.

The speckle field is produced by scattering a Fourier transform intensity distribution off the rough surface of the rotating LSD. A CVI NCBS-633-100 non-polarizing cube beam splitter directs the spatial spectrum to the rotating LSD and reflects the scattered light to the photodiode receiver. We used 10-degree reflective POC LSD attached to the rotating medium of a Quantum Fireball ST hard disk drive. We designed the diffuser to rotate at about 920 cycles/s. Therefore, the linear speed in the vicinity of the illumination spot is 116 m/s. The characteristic illumination spot size on the rough surface is in the range 0.1 to 0.5 mm, yielding a photocurrent fluctuation cutoff frequency of 200 to 1200 kHz. Figure 12 shows oscillograms of the photodiode current for two focusing distances: the focused input image (corresponding to the small speckle size in Figure 8(a)) and unfocused image (corresponding to the large speckle size in Figure 8(b)). It can be seen that the photocurrent spread varies with the image quality, as described by Eq. (4). These results show the feasibility of the image quality analyzer and demonstrate satisfactory performance of the IQA system.

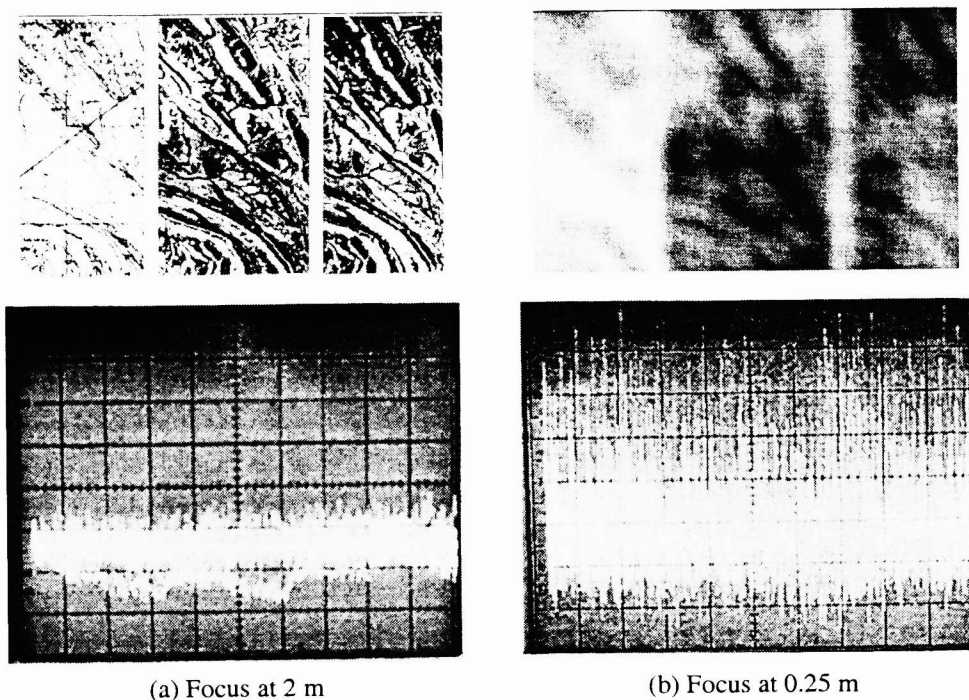


Figure 12. Input images and corresponding oscilloscope traces of the photodiode output for two focusing settings of the input camera.

ACKNOWLEDGEMENTS

This work was supported by the U.S. Army Research Laboratory under Contract DAAD17-99-C-0029.

REFERENCES

1. M.A. Vorontsov, G.W. Carhart, D.V. Pruidze, J.C. Ricklin, and D.G. Voelz, "Image quality criteria for an adaptive imaging system based on statistical analysis of the speckle field," *J. Opt. Soc. Am. A*, Vol. 13, No. 7, pp. 1456-1466, July 1996.
2. M.A. Vorontsov, G.W. Carhart, D.V. Pruidze, J.C. Ricklin, and D.G. Voelz, "Adaptive imaging system for phase-distorted extended source and multiple-distance objects," *Applied Optics*, Vol 36, No. 15, pp. 3319-3328, 1997
3. V.P. Sivokon and M.A. Vorontsov, "High-resolution adaptive phase distortion suppression based solely on intensity information," *J. Opt. Soc. Am. A*, Vol. 15, No. 1, pp. 234-247, January 1998.
4. R.K. Tyson, *Principles of Adaptive Optics*, Academic, Boston, 1991.
5. M.C. Roggemann and B.M. Welsh, *Imaging through Turbulence*, CRC Press, Boca Raton, FL, 1996.
6. G.B. Love, J.S. Fender, and S.R. Restaino, "Adaptive wavefront shaping with liquid crystals," *Opt. Photon. News*, Vol. 6, pp. 16-21, October 1995.
7. R. Dou and M.K. Giles, "Phase measurement and compensation of a wavefront using a twisted nematic liquid-crystal television," *Appl. Optics*, Vol. 35, pp. 3647-3652, 1996.
8. A. Serrano-Heredia, G. Lu, P. Purwosumarto, and F.T.S. Yu, "Measurement of the phase modulation in liquid crystal television based on the fractional-Talbot effect," *Opt. Eng.* 35, 2680-2684, 1996.
9. C. Soutar, S.E. Monroe, Jr., and J. Knopp, "Measurement of the complex transmittance of the Epson liquid crystal television," *Opt. Eng.*, Vol. 33, pp. 1061-1068, 1994.
10. J.M. Younse, "Mirrors on a chip," *IEEE Spect.* Vol. 30, pp. 27-31, Nov. 1993.
11. G.V. Vdovin and P.M. Sarro, "Flexible mirror micromachined in silicon," *Appl. Opt.* Vol. 34, pp. 2968-2972, 1995.
12. M.A. Vorontsov, G.W. Carhart, and J.C. Ricklin, "Adaptive phase-distortion correction based on parallel gradient-descent optimization," *Optics Letters*, Vol. 22, No. 12, pp. 907-909, June 1997.
13. G.W. Carhart, J.C. Ricklin, V.P. Sivokon, and M.A. Vorontsov, "Parallel perturbation gradient descent algorithm for adaptive wavefront correction," in *Adaptive Optics and Applications*, R. Tyson and R. Fugate (Eds.), Proc. SPIE, 3126, 221-227, 1997.
14. G. Cauwenberghs, "A fast stochastic error-descent algorithm for supervised learning and optimization," in *Advances in Neural Information Processing Systems*, San Mateo, CA: Morgan Kaufman, 5, 244-251, 1993.
15. G. Cauwenberghs, "Analog VLSI Stochastic Perturbative Learning Architectures," *Int. J. Analog Integrated Circuits and Signal Processing*, 13, March, 195-209, 1997.
16. J. Alspector, R. Meir, B. Yuhua, and A. Jayakumar, "A Parallel Gradient Descent Method for Learning in Analog VLSI Neural Networks," in *Advances in Neural Information Processing systems*, San Mateo, CA: Morgan Kaufman, 5, 836-844, 1993.
17. D.B. Kirk, D. Kerns, K. Fleischer, and A.H. Barr, "Analog VLSI Implementation of Multi-Dimensional Gradient Descent," in *Advances in Neural Information Processing Systems*, San Mateo, CA: Morgan Kaufman, 5, 789796, 1993.
18. J.W. Goodman, *Introduction to Fourier Optics*, 2nd Edition, McGraw-Hill, New York, 1996.
19. J.W. Goodman, *Statistical Optics*, Wiley, NY, 1985.
20. Light Shaping Diffusers, LSD Circular Kit, Physical Optics Corporation, <http://www.poc.com>.
21. M.A. Vorontsov, "Adaptive wavefront correction with self-organized control system architecture," SPIE, Vol. 3432, *Artificial Turbulence for Imaging and Wave Propagation*, J.D. Gonglewski and V.A. Mikhail (Eds.), pp. 68-72, 1998.